A theoretical and experimental study of hyperbolic and degenerate mixing regions in a chaotic Stokes flow

By W. W. HACKBORN[1], M. E. ULUCAKLI[2] AND T. YUSTER[3]

[1] Department of Mathematics, Augustana University College, Camrose AB, T4V 2R3, Canada
[2] Department of Mechanical Engineering, Lafayette College, Easton, PA 18042, USA
[3] Department of Mathematics, Lafayette College, Easton, PA 18042, USA

We examine the *rotor–oscillator flow*, a slow viscous flow between long parallel plates driven by the rotation of a slender cylinder (the rotor) and the longitudinal oscillation of one of the plates (the oscillator). For rotor locations of interest to us, this flow exhibits a hyperbolic mixing region, characterized by homoclinic tangling associated with a hyperbolic fixed point, and a degenerate mixing region, characterized by heteroclinic tangling associated with two degenerate fixed points on one of the boundary plates (normally the oscillator). These mixing regions are investigated both theoretically, by applying various dynamical tools to a mathematical model of the flow, and experimentally, by observing the advection of a passive tracer in a specially constructed apparatus. Although degenerate mixing regions have been largely ignored or undervalued in previous research on chaotic mixing, our results demonstrate that more mixing is associated with the degenerate mixing region than the hyperbolic one in many cases. We have also discovered a peculiar phenomenon, which we call *Melnikov resonance*, involving a rapid fluctuation in the size of the hyperbolic mixing region as the frequency of the oscillator is varied.

1. Introduction

In recent years, the chaotic advection of fluid particles in a deterministic flow field has been a subject of abiding interest. Most studies of chaotic advection in two-dimensional Stokes flows have used either the geometry of a journal bearing (e.g. Aref & Balachandar 1986; Chaiken *et al.* 1986; Swanson & Ottino 1990; Kaper & Wiggins 1993) or that of a rectangular cavity (e.g. Chien, Rising & Ottino 1986; Leong & Ottino 1989). In studies of this kind, a steady Stokes flow is perturbed by moving one or more of its boundaries in a periodic way. The resulting flow may exhibit a *hyperbolic mixing region*, associated with a hyperbolic stagnation point in the unperturbed flow, or a *degenerate mixing region*, associated with a pair of points on a boundary at which the unperturbed flow separates and reattaches. One of the few studies to have considered a degenerate mixing region (but only as a very small part of a much larger study) is that of Jana, Metcalfe & Ottino (1994*a*). The term *mixing* is used here in a *dynamical systems* sense like that of Aref (1991); a mixing region is determined by a tangle of invariant manifolds associated with fixed points of a Poincaré map related to the flow.

In this paper, we conduct a theoretical and experimental study of chaotic advection in a new setting: the *rotor–oscillator flow*. The theoretical rotor–oscillator flow is a two-dimensional Stokes flow bounded by two infinite parallel plates and induced by a line

rotlet (the rotor) and the longitudinal oscillation of one of the plates (the oscillator). A line rotlet is a singularity representing a rotating cylinder of infinitesimal radius and is mathematically identical to a line vortex of potential flow theory. The time-periodic perturbation caused by the motion of the oscillator is assumed to be small in magnitude. To investigate the rotor–oscillator flow experimentally, we designed and constructed an apparatus to physically simulate the theoretical flow. This apparatus consists of a rectangular cavity in which flow is induced by the rotation of a thin cylindrical shaft and the oscillation of one of the long sidewalls; the fluid used in the apparatus is a sugar solution, an inexpensive alternative to the glycerine used in most chaotic Stokes flow experiments to date. For rotor locations of interest to us, the *rotor–oscillator flow* (in theory and in our experiments) has a hyperbolic mixing region, a degenerate mixing region, and, when these two regions overlap, a hybrid mixing region.

The primary aim of our research is to investigate the mixing regions of the rotor–oscillator flow both theoretically and experimentally. A related objective is to compare theoretical predictions about the mixing regions to experimental observations of them. The basis of this comparison is the size and shape of the regions since these two characteristics can be visualized experimentally. Hence, the only dynamical tools we apply to the theoretical flow are those that provide information on the observable qualities of the mixing regions. Many of the standard theoretical techniques apply to hyperbolic mixing regions but have not yet been shown to be valid for degenerate mixing regions; we address some of the issues of validity in this paper. The mixing regions in our experiments are visualized by injecting dye at specific points and subsequently recording the time evolution of the dye pattern via photography.

2. The theoretical flow

We consider a two-dimensional incompressible flow between infinite parallel plates driven by the rotation of a cylinder (the rotor) parallel to the plates and by the longitudinal oscillation of one of the plates (the oscillator). Let (x, y, z) be Cartesian coordinates and t be time. Assume the plates coincide with the planes $x = -h$ and $x = h$ and the axis of the rotor coincides with the line $(x, y) = (c, 0)$, where $-h < c < h$. The rotor has radius a and rotates counterclockwise with angular velocity ω. The plate at $x = h$ oscillates in the y-direction with velocity $V \cos(\alpha t)$ while the other plate is fixed. Taking h as a characteristic length, $a^2\omega/h$ as a characteristic flow velocity (since V is comparatively small in our experiments), and $\alpha/2\pi$ as a characteristic oscillatory frequency, the Reynolds and Strouhal numbers for the flow are

$$Re = \frac{a^2\omega}{\nu}, \quad Sr = \frac{h^2\alpha}{2\pi a^2\omega}, \tag{2.1}$$

respectively, where ν is the kinematic viscosity of the fluid. We assume that $Re \ll 1$ and $Sr = O(1)$ to restrict the flow to the quasi-steady Stokes regime. Finally, we let $a \to 0$ while holding $a^2\omega$ constant so that the force exerted by the rotor on the fluid approaches zero but the torque remains constant. The resulting flow is the superposition of a steady flow due to a line rotlet between fixed parallel plates and a time-periodic Couette shear flow induced by the oscillator; let ψ denote the stream function for the steady flow. We convert to non-dimensional quantities as follows:

$$\frac{x}{h} \to x, \quad \frac{y}{h} \to y, \quad \frac{c}{h} \to c, \quad \frac{\psi}{a^2\omega} \to \psi, \quad \frac{ta^2\omega}{h^2} \to t. \tag{2.2}$$

In terms of these quantities, the boundary plates coincide with $x = -1$ and $x = 1$, and the line rotlet coincides with $(x, y) = (c, 0)$, where $-1 < c < 1$. The equations governing particle advection in the flow are

$$\frac{\mathrm{d}x}{\mathrm{d}t} = -\frac{\partial \psi}{\partial y}, \quad \frac{\mathrm{d}y}{\mathrm{d}t} = \frac{\partial \psi}{\partial x} + \epsilon(1 + x) \cos(\lambda t), \tag{2.3}$$

where

$$\epsilon = \frac{Vh}{2a^2\omega}, \quad \lambda = \frac{h^2 a}{a^2 \omega}. \tag{2.4}$$

The stream function ψ is given by (Hackborn 1990)

$$\psi = \tfrac{1}{2}\log[F(x, y)] + \int_0^\infty G(x, k)\cos(ky)\,\mathrm{d}k, \tag{2.5}$$

where

$$F(x, y) = \frac{1 - 2\,\mathrm{e}^{\pi y/2}\cos[\tfrac{1}{2}\pi(x - c)] + \mathrm{e}^{\pi y}}{1 + 2\,\mathrm{e}^{\pi y/2}\cos[\tfrac{1}{2}\pi(x + c)] + \mathrm{e}^{\pi y}} \tag{2.6}$$

and

$$G(x, k) = \frac{2[\tanh k \cosh(kx) - x \sinh(kx)]\cosh(kc)}{\sinh(2k) + 2k}$$

$$+ \frac{2[\coth k \sinh(kx) - x \cosh(kx)]\sinh(kc)}{\sinh(2k) - 2k}. \tag{2.7}$$

3. The experimental apparatus

The experimental apparatus is shown in figure 1. The test cell dimensions were chosen to maintain a reasonably large length-to-width ratio (about 4:1) in order to correspond with the infinitely long parallel walls of our theoretical flow. The rectangular cavity is 40.6 cm long, 10.2 cm wide, and 10.2 cm deep. A vertically oriented cylindrical shaft of diameter 0.6 cm located at $c/h = 0.49$ serves as the rotor.

In order to use the Stokes approximation, we required that $Re < 1$. We then calculated the allowable range for the angular velocity of the rotor based on the experimentally determined kinematic viscosity of the test fluid, which was found to be about $\nu = 9$ cm^2 s^{-1}. Ballal & Rivlin (1976) found that, for $Re = 4$ in various protocols, the inclusion of inertial effects had a minimal impact on streamlines in general and that hyperbolic stagnation points and their associated manifolds seemed particularly resistant to such effects. Moreover, when the rotor and oscillator were halted, the fluid came to rest virtually immediately, as should be the case in a Stokes flow. Thus, the Stokes approximation was expected to be reliable for $Re < 1$. For the majority of our experiments, $Re < 0.5$.

A perturbation was imposed on the flow by oscillating the side $x = h$ in its plane with a velocity of $V\cos(\alpha t)$. Note that $V = \alpha d$, where d is the amplitude of the oscillation. In order to keep $Sr = O(1)$, we ran experiments with $d = 1.65$ and 5 mm, and allowed α to vary between 0.1 and 0.4 rad s^{-1}.

Our test fluid consisted of sugar dissolved in water (and a small amount of lemon juice to inhibit crystallization). The solution was 75% sugar by weight and had a dynamic viscosity of 1.345 Pa s and a density of 1.48 g cm^{-3} at 23 °C.
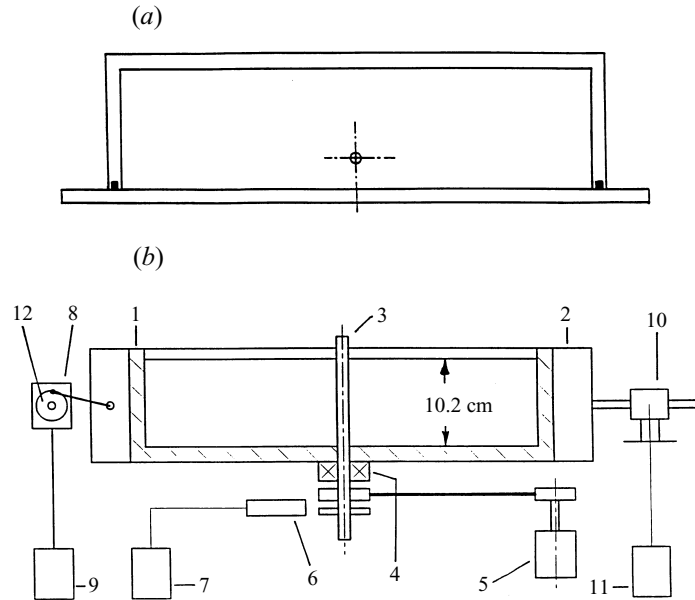
(*a*)

(*b*)

FIGURE 1. Schematic of (*a*) the plan view of the test cavity, and (*b*) the test facility: 1, test vessel; 2, oscillating boundary; 3, rotating cylinder; 4, bearing; 5, rotor motor; 6, magnetic pick-up; 7, electronic counter; 8, oscillator driver motor; 9, DC power supply; 10, linear variable differential transformer; 11, oscilloscope; 12, oscillator crank mechanism.

A mixture of sugar solution and Rhodamine Red liquid dye which was matched to the density of our sugar solution was used as the tracer in the experiments. There was no visual evidence of diffusion of the dye into the sugar solution during various tests of average length 45 minutes and at room temperature (22–23 °C), nor did the dye rise or sink significantly.

4. Sources of difference between theoretical and experimental flows

In this section, we examine potential sources of difference between the theoretical flow and that generated by the experimental apparatus. We consider the non-zero size of the rotor, the non-zero Reynolds number, bottom effects, surface effects, and effects due to the endwalls in the apparatus. To assess the magnitudes of these factors, we ran tests using our apparatus in the steady ($\epsilon = 0$) configuration and made comparisons between our observations and the steady theoretical flow. Throughout this and subsequent sections, the non-dimensional versions of x, y and c are used, see (2.2).

In our apparatus, the rotor is centred at $x = 0.49$ on the x-axis. Theory predicts that the hyperbolic stagnation point A_0 (see figure 2) of the steady flow should be found at $x = -0.638$, but experimentally we located this point at approximately $x = -0.45$. Let Δ be $x_{observed} - x_{predicted}$ for the hyperbolic stagnation point. When we experimented with various size rotors, we found Δ to be a positive increasing function of the rotor diameter. Thus we are confident that the non-zero rotor size does significantly affect the experimental flow. Owing to constructional constraints, the smallest rotor diameter we were able to realize was 0.6 cm.

When we looked at streamlines of the steady flow generated by our apparatus for Reynolds numbers between 0.5 and 1, a slight asymmetry was apparent. The symmetry
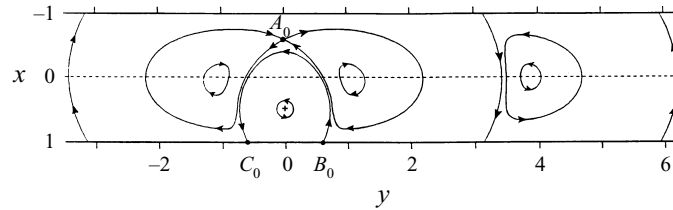
FIGURE 2. Points A_0, B_0, and C_0 and significant streamlines of the steady flow for $c = 0.5$. The position of the line rotlet is indicated by $+$.

of the theoretical streamlines depends heavily on the zero Reynolds number. As none of the other sources of difference we have mentioned should cause an asymmetry, we ascribe it to the non-zero Reynolds number.

The magnitudes of the bottom, end, and surface effects seem to be small. Experiments with dye in a partially filled tank indicated that dye very near the bottom of the tank is affected by proximity to the bottom, but that there was no effect correlating with depth in a fully filled tank once the dye was injected well away from the bottom; this confirms observations made in Swanson & Ottino (1990). It also seems likely that the end effects are not significant due to the extreme slowness of the theoretical flow in the regions close to the endwalls of the experimental apparatus. When the dye was allowed to reach the surface, the size and shape of the streamlines were noticeably affected. But as long as the dye remained below the surface, we were not able to observe any difference in the shapes or sizes of streamlines as a function of how close to the surface the dye was injected. Thus we believe that the surface effects are also minimal.

It thus seems likely that the major source of difference between the theoretical and experimental flows is the non-zero size of the rotor. We felt this difference was large enough to justify adjusting the parameter c of the theoretical flow to account for the difference. We measured the locations of the points A_0, B_0, and C_0 (see figure 2) in the steady experimental flow and the shapes and sizes of the stagnation streamlines associated with them, and compared those measurements to the predictions of the steady theoretical flow for various values of c. We found that the 'best match' for the experimental flow ($c = 0.49$) was the theoretical flow with $c = 0.54$. In §6, we will be comparing theoretical predictions made with $c = 0.54$ to our experimental results.

5. Theoretical predictions

The theoretical flow represented by equations (2.3), together with (2.5) to (2.7), will be analysed in this section. Section 5.1 presents some preliminary ideas and definitions. In §§5.2–5.5, we apply some of the standard theoretical tools: Poincaré sections, invariant manifolds, Melnikov's method, and lobe dynamics. The primary goals of this section are to understand the dynamics of the theoretical flow (particularly those aspects of the dynamics that relate to mixing regions) and to compare the kinds of information provided by the various theoretical techniques.

5.1. *Preliminary considerations*

Our theoretical flow has three parameters: c, indicating the position of the rotlet; and ϵ and λ, governing the motion of the oscillator. The steady flow ($\epsilon = 0$) was studied by Hackborn (1990). This flow exhibits a hyperbolic stagnation point A_0 (see figure 2) on the x-axis for values of c in the range $c_1 < c < c_2$, where $c_1 \approx 0.4411$ and $c_2 \approx 0.6700$.
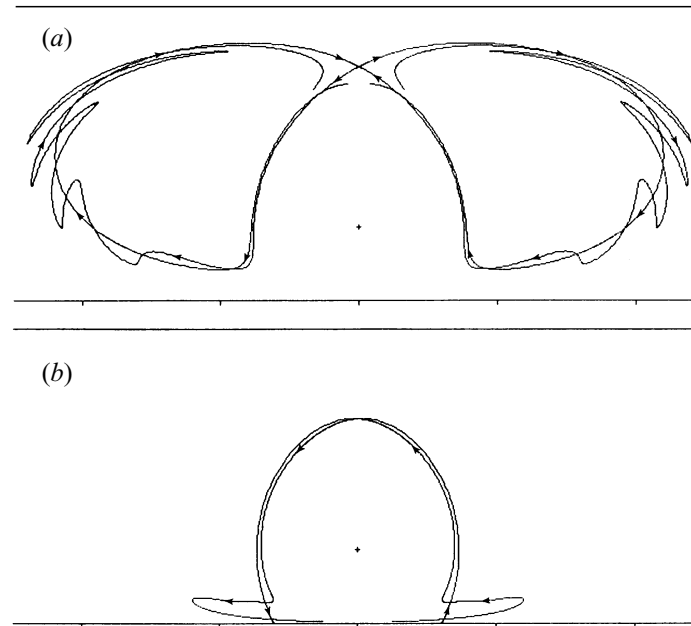
(*a*)

(*b*)

FIGURE 3. Short segments of key invariant manifolds for $c = 0.5$, $\epsilon = 0.004$, and $\lambda = 0.4$: (*a*) the stable and unstable manifolds A_s and A_u of the hyperbolic fixed point A; (*b*) the unstable and stable manifolds B_u and C_s of the degenerate fixed points B and C. The arrows on the manifolds indicate the direction of point movement under iteration of P.

A figure-eight pair of homoclinic streamlines is attached to A_0. Furthermore, for $c_1 < c < 1$, a heteroclinic streamline leaves the boundary $x = 1$ at B_0, a separation point, and returns to it at C_0, a reattachment point. The steady flow underlying all theoretical results in this paper is topologically equivalent to that depicted in figure 2.

The steady flow has a sequence of Moffatt eddies (so the flow speed is exponentially small as $|y| \to \infty$) at each end of the flow domain (see Moffatt 1964). These eddies, and the associated separation and reattachment points, are ignored here since they occur beyond the bounds of the finite tank of our experiments.

The unsteady flow, for which $\epsilon \neq 0$, is time-periodic with period $T = 2\pi/\lambda$. Our basic theoretical tool for analysing this flow is the *Poincaré map* P which maps the position of a fluid particle at time $t = 0 \pmod T$ to its position one period later. P is area-preserving (since the underlying flow is incompressible), and it has a time-reversal symmetry about the x-axis, i.e. $P^{-1} = S_x P S_x$ where S_x denotes reflection in the x-axis (Jana *et al.* 1994*a*).

If $\epsilon = 0$, P will be denoted by P_0. The stagnation point A_0 of the steady flow is a hyperbolic fixed point of P_0, and the *stable* and *unstable manifolds* of A_0 under P_0 coincide with the homoclinic streamlines attached to A_0. A standard lemma (see Guckenheimer & Holmes 1983) ensures that, for $|\epsilon|$ sufficiently small, P has a locally unique hyperbolic fixed point A, possessing stable and unstable manifolds A_s and A_u respectively, within an $O(\epsilon)$ distance of A_0. Owing to the symmetry of P, A_s and A_u are mirror images of each other in the x-axis. See figure 3(*a*).

Under P_0, B_0 has an unstable manifold and C_0 a stable manifold coinciding with the heteroclinic streamline joining B_0 and C_0 in the steady flow. Although there is no general theory dealing with perturbations of degenerate (non-hyperbolic) fixed points such as B_0 and C_0, we have proven that, for $|\epsilon|$ sufficiently small, P has degenerate fixed

points B and C (arising from B_0 and C_0) with unstable and stable manifolds B_u and C_s respectively. This proof is given in Yuster & Hackborn (1997) and is outlined here. An analysis of the flow near B_0 shows that the only candidate for B has coordinates $(1, b)$ where b is the smallest positive value such that

$$\int_0^T \psi_{xx}\left(1, b + 2\frac{\epsilon}{\lambda}\sin(\lambda t)\right)\mathrm{d}t = 0. \tag{5.1}$$

For small $|\epsilon|$, (5.1) has a solution $b = b_0 + O(\epsilon^2/\lambda^2)$ where b_0 is the y-coordinate of B_0. One now defines a region $\varDelta$ bounded by a triangle with one vertex at B and two vertices in the fluid such that for $S \subseteq \varDelta$, $\mathscr{P}(S) = P(S) \cap \varDelta$ is similar to a contraction map. The iterates of $\varDelta$ under $\mathscr{P}$ converge to an initial segment of B_u, and this implies the global existence of B_u. (Note: we used this method when computing B_u.) Both C and C_s are obtained from B and B_u by reflection about the x-axis. See figure 3(b).

5.2. *Poincaré sections*

To simulate our dye advection experiments (see §6), the Poincaré sections considered here were created by iterating P on initial points lying on two small circles – one centred at A and the other at a point near B. In figure 4(a), 500 iterations and five initial points on each of the two small circles were used.

The regions strewn with points in figure 4(a) roughly correspond to mixing regions. As will be seen in §§5.3 and 5.4, these mixing regions are associated with A, B, and C and the tangling of their invariant manifolds. For a fixed (non-zero) λ and sufficiently small $|\epsilon|$, there are two distinct mixing regions: a *hyperbolic mixing region* associated with A and a *degenerate mixing region* associated with B and C. As $|\epsilon|$ increases, these two mixing regions begin to intersect to form a *hybrid mixing region*. It would appear from figure 4(a) that a hybrid mixing region exists for the parameters of parts (i) to (iii) but does not exist for the parameters of part (iv); more will be said about this in §5.3.

Regular regions, comprising narrow *stochastic bands* bounded by *KAM tori* (see Guckenheimer & Holmes 1983), are associated with P for $|\epsilon|$ sufficiently small and non-zero. Such a region is separated from an adjacent mixing region by a KAM torus (through which fluid motion via P is impossible). Regular regions surrounding the rotlet and two elliptic fixed points which persist from the unperturbed flow can be seen in figure 4(a). A fourth regular region encircles the hyperbolic mixing region when no hybrid mixing region exists. *Islands* (see Kaper & Wiggins 1993) may also exist in some cases.

Long-term Poincaré sections, such as those of figures 4(a), are well-suited for visualizing the asymptotic structure of a chaotic flow, but they are less suitable for portraying a short-term dye advection experiment. Poincaré sections created using fewer iterations but more initial points can better simulate such an experiment. In figure 4(b), 50 iterations were used with 50 initial points on the same two small circles (clearly visible in the figure) and for the same four sets of parameter values as in figure 4(a). Note the rather striking differences between parts (iii) and (iv) of figure 4(b) and the corresponding parts of figure 4(a).

Short-term Poincaré sections such as ours are similar to the blob deformation simulations of Jana *et al.* (1994a) in which a set of points, representing a blob, is plotted, for example, after periods 2 to 5 to visualize the deformed blob after five periods. In figure 4(b), an initial blob is represented only by points on its boundary, and points are plotted starting at period 0.

When constructing Poincaré sections, points are often reflected about an axis of symmetry (e.g. Swanson & Ottino 1990). However, when the orbit of a Poincaré map

is reflected in an axis of time-reversal symmetry, its image is a time-reversed orbit whose initial point is therefore unknown. Reflection in the x-axis was not used in the Poincaré sections of figure 4 since we wanted to control the positions of initial points.

In the numerical integration of (2.3), each integral in a partial derivative of ψ was computed, as needed, using a tail integral estimate and a quadrature calculation involving about 20 integrand evaluations on average. Thus, computation of P required considerably more work than would be needed if ψ were available in closed form. Nevertheless, computation time for a Poincaré section averaged only about fifteen minutes on a Sun Sparcstation 10.

5.3. *Invariant manifolds*

The invariant manifolds associated with A, B, and C allow us to precisely define the mixing regions introduced in §5.2. Consider first the hyperbolic fixed point A. It is shown in §5.4 that, for sufficiently small $|\epsilon|$, the manifolds A_s and A_u intersect transversely infinitely many times to form a double *homoclinic tangle*. Following Wiggins (1992), a point N on corresponding half-manifolds of A_s and A_u (i.e. arising from the same homoclinic streamline in the steady flow) is a *primary intersection point* (pip) if the segments of A_s and A_u from A to N intersect only at A and N. The region bounded by the segments of A_s and A_u joining two adjacent pips is a *lobe*. (Secondary intersection points occur when lobes intersect. Figure 3 shows only pips.) Since A_s and A_u are invariant under P, P maps a lobe to another lobe. The *hyperbolic mixing region* is defined as the union of all lobes associated with A. Now consider the degenerate fixed points B and C. Results from §5.4 indicate that, for sufficiently small $|\epsilon|$, B_u and C_s intersect transversely infinitely many times to form a *heteroclinic tangle*. In this case, a point N on both B_u and C_s is a pip if the segment of B_u from B to N and the segment of C_s from C to N intersect only at N; the region bounded by the segments of B_u and C_s joining two adjacent pips is a lobe. The *degenerate mixing region* is defined as the union of all lobes associated with B and C.

Our numerical experiments indicate that if λ is held fixed and $|\epsilon|$ is made large enough, A_s and B_u (and also, by symmetry, A_u and C_s) intersect. Suppose N is a point on both A_s and B_u. The image of N under P or P^{-1} also lies on A_s and B_u, and the orbits of P and P^{-1} based at N approach A and B respectively. In cases where A_s and B_u meet in this complicated way, we define the *hybrid mixing region* to be the union of the hyperbolic and degenerate mixing regions. The eventual intersection of initially isolated mixing regions to form a hybrid region as a parameter is increased can also be seen in other studies of chaotic advection (e.g. Aref 1984).

Although long-term Poincaré sections like those in figure 4(*a*) with initial points on small circles near A and B can be used to indicate the existence of a hybrid mixing region, their reliability for this purpose is suspect since their appearance can vary significantly with the size of the small circles, the number of initial points, and the number of iterations. In theory, one can reliably detect a hybrid mixing region by computing segments of A_s and B_u long enough to intersect. Figure 5(*a*), for example, confirms that a hybrid region exists in one case (cf. figure 4(*a*)(i)). However, figure 5(*b*) depicts another case in which very long segments of A_s and B_u (requiring about 36 hours of computation) do not intersect even though figure 4(*a*)(iii) suggests that a hybrid region exists in this case. (Even longer segments of A_s and B_u which took weeks to compute failed to cross.) A more efficient, but still reliable, way to detect a hybrid mixing region is to compute a Poincaré section with initial points placed on B_u near B using enough iterations so that some iterate of an initial point lies inside a lobe formed by A_s and A_u. This technique was used with 500 iterations (see figure 5*c*) to
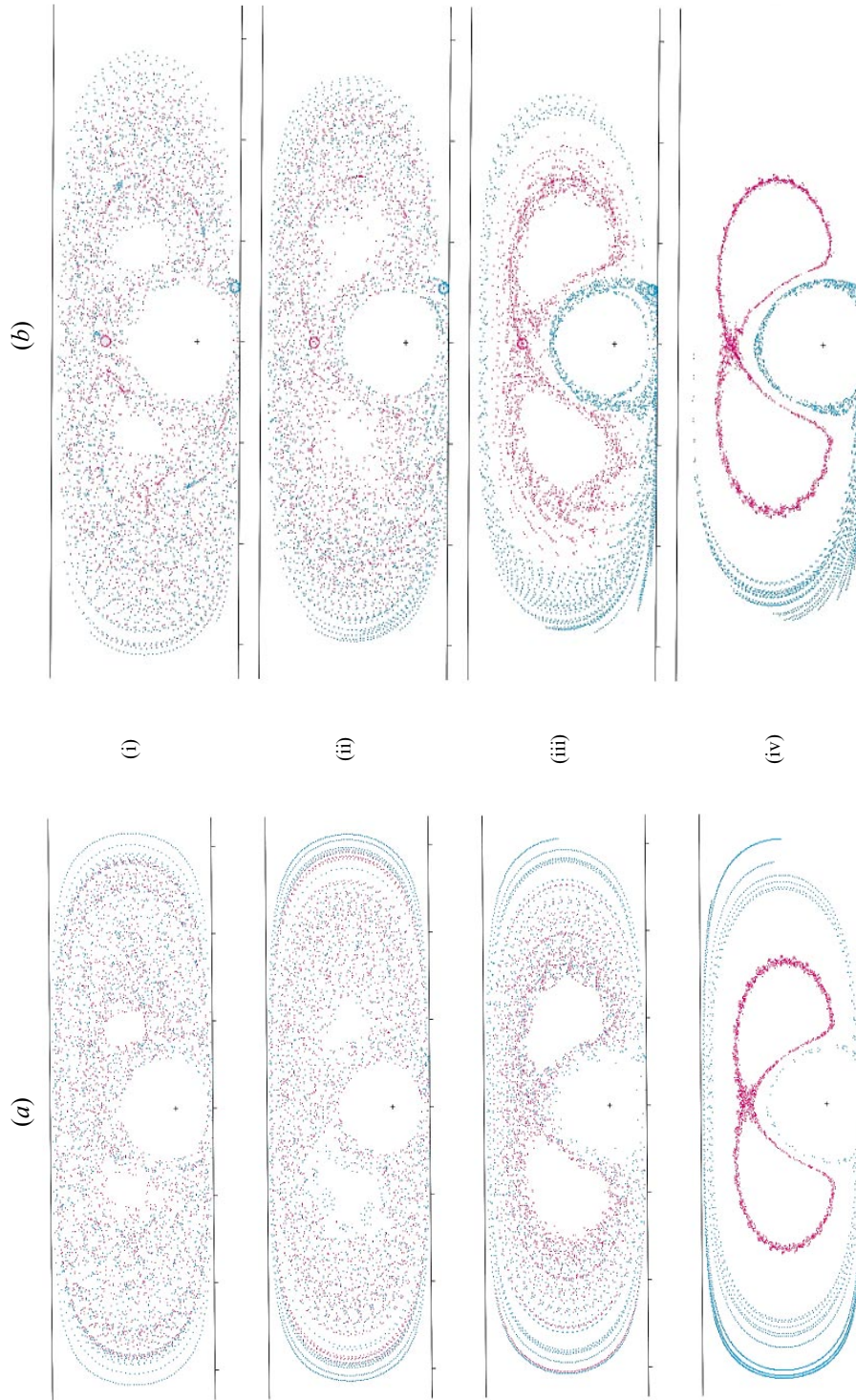
FIGURE 4. (*a*) Poincaré sections using 500 iterations and 5 initial points near each of points *A* and *B*, with $c = 0.54$: (i) $\epsilon = 0.02$, $\lambda = 0.406$; (ii) $\epsilon = 0.04$, $\lambda = 0.813$; (iii) $\epsilon = 0.02$, $\lambda = 1.232$; (iv) $\epsilon = 0.04$, $\lambda = 2.463$. Points initially near *A* and *B* and their iterates are coloured red and blue, respectively. (*b*) As (*a*) but short-term Poincaré sections using 50 iterations and 50 initial points near each of points *A* and *B*.
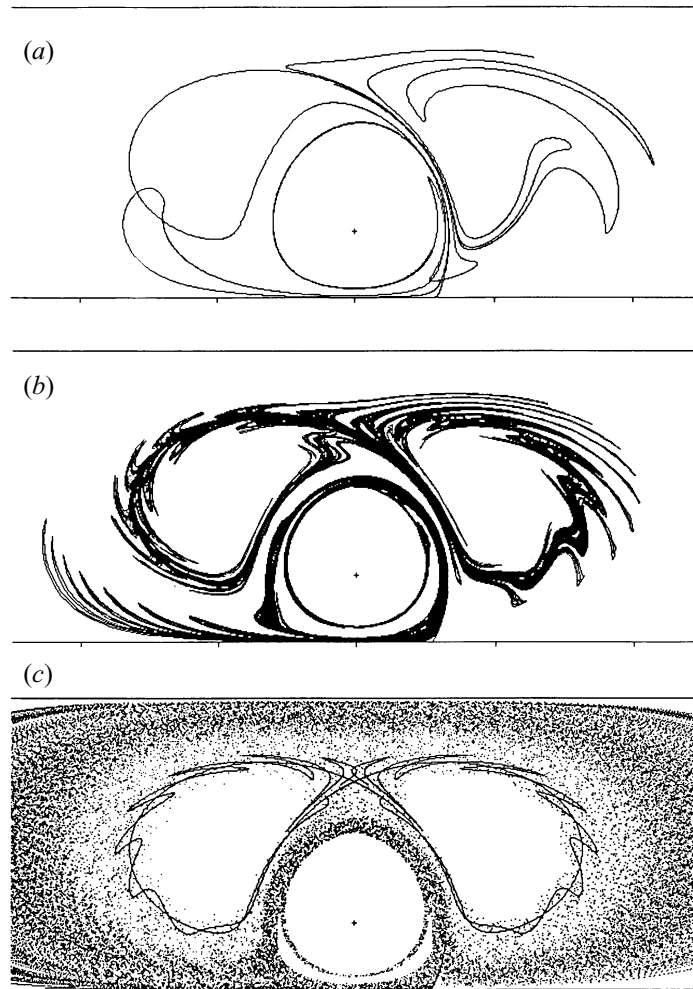
(a)

(b)

(c)

FIGURE 5. Detection of a hybrid mixing region. (*a*) Segments of the manifolds A_s and B_u intersect for $c = 0.54$, $\epsilon = 0.02$, $\lambda = 0.406$, confirming the existence of a hybrid mixing region. (*b*) Very long segments of A_s and B_u fail to intersect for $c = 0.54$, $\epsilon = 0.02$, $\lambda = 1.232$. (*c*) Poincaré section using 500 iterations and 100 initial points on B_u near point B and short segments of A_s and A_u for $c = 0.54$, $\epsilon = 0.02$, $\lambda = 1.232$. Some points of the Poincaré section lie inside lobes formed by A_s and A_u, confirming the existence of a hybrid mixing region.

confirm the existence of a hybrid region for the parameters of figure 4(*a*)(iii). When 2500 iterations were used, this technique revealed that a hybrid region exists even for the parameters of figure 4(*a*)(iv) which exhibits no trace of such a region. This latter case shows that transport between subregions of a hybrid mixing region may require a very long time.

The manifolds A_u and B_u coincide with the streaklines obtained experimentally by injecting tracer dye at A and B respectively. Many studies of chaotic mixing (e.g. Swanson & Ottino 1990) have further noted that a blob of tracer dye on or near an unstable manifold tends increasingly to conform to that manifold as time proceeds. Hence, unstable manifolds assist greatly in flow visualization. Figure 6 depicts segments of A_u and B_u for the same four sets of parameter values as those used in figure 4.
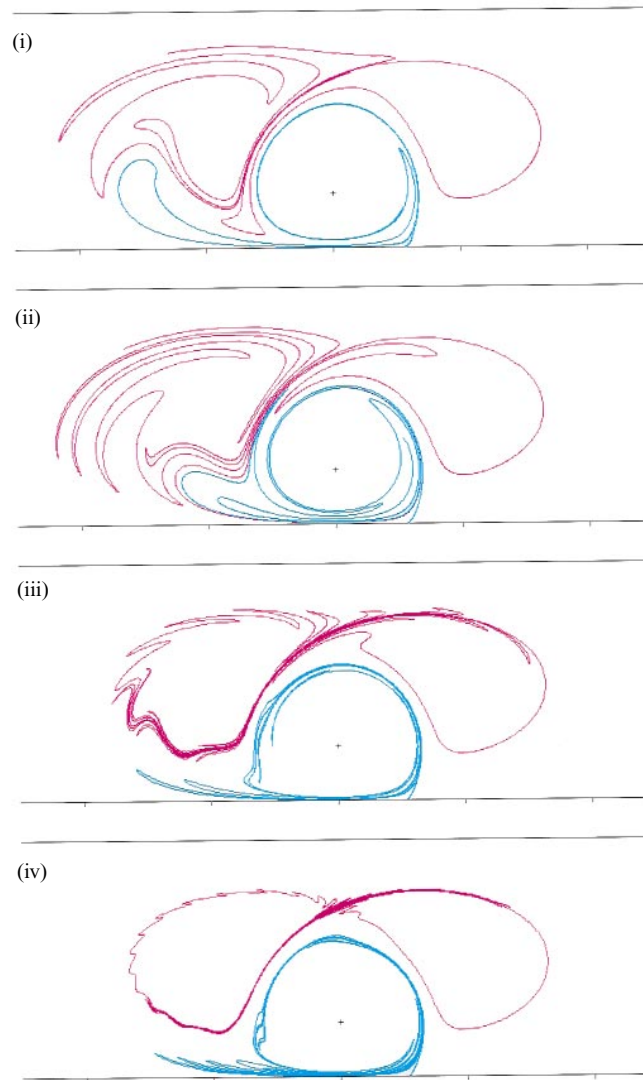
FIGURE 6. Segments of the unstable manifolds A_u (shown in red) and B_u (shown in blue) for $c = 0.54$: (i) $\epsilon = 0.02$, $\lambda = 0.406$; (ii) $\epsilon = 0.04$, $\lambda = 0.813$; (iii) $\epsilon = 0.02$, $\lambda = 1.232$; (iv) $\epsilon = 0.04$, $\lambda = 2.463$.

Some general remarks should be made on mixing regions and periodic points. Let P be the Poincaré map associated with a time-periodic Stokes flow, and let M be a region of finite area comprising (like our hyperbolic or degenerate mixing region) all lobes formed by a homoclinic or heteroclinic tangle associated with one or two fixed points of P. Clearly, $P: M \rightarrow M$. We make the reasonable assumption that P mixes in Aref's DS sense (see Aref 1991) in M. It follows that any subset of M of positive measure invariant under P, or an iterate of P, is identical (up to a set of measure zero) to M. Thus, M is identical in this way to the region comprising all lobes formed by the homoclinic tangle associated with any hyperbolic period point of P lying in M, and so our hyperbolic or degenerate mixing region (if it has finite area) could be defined using the manifolds of any hyperbolic periodic point within it. (The *Smale–Birkhoff Homoclinic Theorem*, see Guckenheimer & Holmes 1983, implies that a countable infinity of hyperbolic periodic points exists in our hyperbolic mixing region; this is

probably also true of our degenerate mixing region.) However, the unstable manifolds visualized in dye advection experiments tend to be those on which the stretching is largest. Generally, the stretching on the unstable manifold of a particular period-1 (fixed) point (especially one that persists from the unperturbed flow, like A, B, and C in our study) exceeds that of other periodic points. Manifolds of period-1 points also yield more information on flow transport (see §5.5) than those of higher-order periodic points since the former relate to the Poincaré map itself rather than iterations of it. For these reasons, our use of manifolds associated with A, B, and C to define and analyse our mixing regions is very appropriate.

Our manifolds were computed using a modified version of an algorithm from Parker & Chua (1989). This algorithm adaptively maintains an array of points representing an advancing portion of the manifold. Computation time for segments of both A_u and B_u as in figure 6 averaged about an hour on a Sun Sparcstation 10.

5.4. *Melnikov's method*

To employ Melnikov's method (see Wiggins 1988) in our case, (2.3) must be expressed in the form $\dot{x} = f(x) + \epsilon g(x, t)$, where x, f, and g are vectors in $\mathbb{R}^2$. Let $q_0(t)$, $t \in (-\infty, \infty)$, be a trajectory homoclinic to A_0 in the unperturbed flow. The signed distance $d(t_0)$ between corresponding half-manifolds of A_s and A_u at the point $q_0(-t_0)$, as measured along a line passing through this point and perpendicular to the curve $q_0(t)$ there, is given by

$$d(t_0) = \epsilon \frac{M(t_0)}{\|f(q_0(-t_0))\|} + O(\epsilon^2), \quad M(t_0) = \int_{-\infty}^{\infty} f(q_0(t)) \wedge g(q_0(t), t + t_0) \, dt, \quad (5.2)$$

where $M(t_0)$ is the Melnikov function and $f \wedge g = f_1 g_2 - f_2 g_1$. For $|\epsilon|$ sufficiently small, simple zeros of $M(t_0)$ correspond to simple zeros of $d(t_0)$ and pips at which A_s and A_u intersect transversely.

There is no general theory dealing with the applicability of Melnikov's method to invariant manifolds associated with degenerate fixed points. To prove the method applies to B_u and C_s, it must be shown that B_u and C_s can be expressed as series in powers of ϵ, up to at least a $O(\epsilon^2)$ error term, on time intervals $(-\infty, 0]$ and $[0, \infty)$, respectively. We have been unable to prove this. Nevertheless, we assume that Melnikov's method does apply to B_u and C_s; some numerical justification is given below. Taking $q_0(t)$ to be a trajectory heteroclinic to B_0 and C_0 in the unperturbed flow, (5.2) now gives the signed distance $d(t_0)$ between B_u and C_s; in this case, simple zeros of $M(t_0)$ correspond to pips at which B_u and C_s intersect transversely for $|\epsilon|$ sufficiently small.

Let $M_H(t_0)$ denote the Melnikov function associated with A_s and A_u, and $M_D(t_0)$ that associated with B_u and C_s. From (2.3) and (5.2),

$$M_H(t_0) = F_H(c, \lambda) \sin(\lambda t_0 - \phi_H), \quad M_D(t_0) = F_D(c, \lambda) \sin(\lambda t_0 - \phi_D), \quad (5.3)$$

where the phase shifts ϕ_H and ϕ_D depend on the location of $q_0(0)$. We take $\phi_D = \pi$ and allow $F_D(c, \lambda)$ to be negative, consistent with choosing $q_0(0)$ for the heteroclinic trajectory to lie on the x-axis. For $|\epsilon|$ sufficiently small, non-zero values of the *Melnikov amplitudes* $F_H(c, \lambda)$ and $F_D(c, \lambda)$ imply homoclinic and heteroclinic tangling respectively, which in turn imply *chaotic dynamics*. See figure 7. Both $M_H(t_0)$ and $M_D(t_0)$ are periodic in t_0 with period $T = 2\pi/\lambda$ and have two simple zeros per period. Thus, if $|\epsilon|$ is small, corresponding half-manifolds of A_s and A_u as well as B_u and C_s intersect at two pips per period. The number of pips per period must be even, but it may be four or more for larger values of $|\epsilon|$.
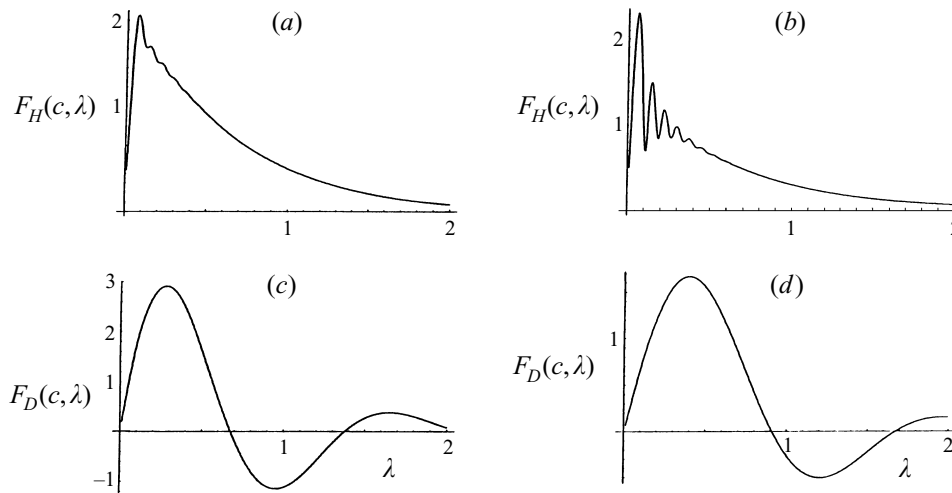
FIGURE 7. Graphs of the Melnikov amplitudes $F_H(c, \lambda)$ and $F_D(c, \lambda)$ versus λ. In (a) and (c), $c = 0.5$; in (b) and (d), $c = -0.5$.

	$\mu(L_H)$		$\mu(L_D)$	
ϵ	Numerical	Melnikov	Numerical	Melnikov
0.001	0.005 90	0.005 88	0.012 25	0.012 31
0.004	0.023 50	0.023 54	0.048 66	0.049 24
0.007	0.041 08	0.041 19	0.081 83	0.086 17
0.010	0.058 62	0.058 84	0.101 63	0.123 10

TABLE 1. Hyperbolic and degenerate lobe areas, $\mu(L_H)$ and $\mu(L_D)$, for $c = 0.5$, $\lambda = 0.4$, and several values of ϵ. Areas are found both numerically and using Melnikov amplitudes.

The integral with respect to arclength of $d(t_0)$ between two adjacent pips gives, to within an $O(\epsilon^2)$ error, the area of the lobe bounded by the manifold segments joining those pips (Rom-Kedar, Leonard & Wiggins 1990). Using (5.2) and (5.3), it follows that

$$\mu(L_H) = 2 \left| \frac{\epsilon}{\lambda} F_H(c, \lambda) \right| + O(\epsilon^2), \quad \mu(L_D) = 2 \left| \frac{\epsilon}{\lambda} F_D(c, \lambda) \right| + O(\epsilon^2), \quad (5.4)$$

for $|\epsilon|$ sufficiently small, where $\mu(L_H)$ denotes the area of a hyperbolic lobe (a lobe bounded by A_s and A_u) and $\mu(L_D)$ the area of a degenerate lobe (a lobe bounded by B_u and C_s).

Some lobe areas, found numerically and also using the leading terms in (5.4), are given in table 1 (cf. figure 3). For each case in table 1, all hyperbolic lobes have equal area, and all degenerate lobes have equal area except when $\epsilon = 0.01$. For $\epsilon = 0.01$, B_u and C_s have four pips per period and, thus, the degenerate lobes are of two sizes; the numerical value of $\mu(L_D)$ in table 1 applies to a large degenerate lobe. The increasingly good agreement between numerical and Melnikov values of $\mu(L_D)$ in table 1 as ϵ decreases provides strong numerical evidence for our assumption that Melnikov's method applies to the manifolds B_u and C_s.

Lobe area is a measure of the rate at which mixing occurs per period. Based on the areas of hyperbolic and degenerate lobes, it is evident from (5.4) and figure 7 (cf. table 1) that more mixing is associated with the degenerate mixing region than the hyperbolic
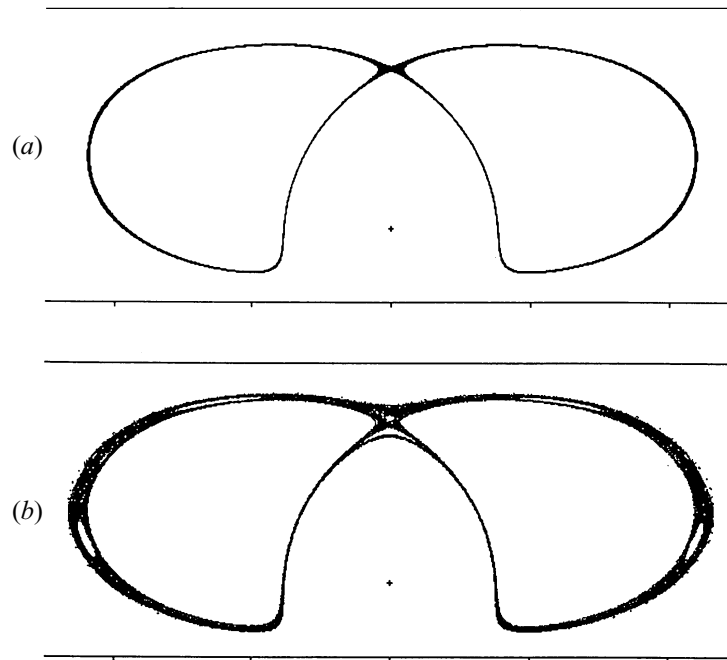
FIGURE 8. Poincaré sections using 5000 iterations and 10 initial points on manifold A_u near point A obtained by oscillating the plate at $x = -1$ for $c = 0.5$ and $\epsilon = 0.0003$: (a) $\lambda = 0.110$, (b) $\lambda = 0.146$.

mixing region in many cases. The mixing associated with the degenerate mixing region is substantial even when $c = -0.5$ (see figure 7d); this is surprising since the manifolds defining the degenerate mixing region are attached to the non-oscillating plate at $x = -1$ in this case. (When $c = -0.5$, points B and C lie on the plane $x = -1$ and coincide with B_0 and C_0.) Our results differ from those of Jana *et al.* (1994a) in their study of the flow due to corotating cylinders inside a larger fixed cylinder. Using Melnikov's method (but only on a small subset of their parameter space), they found the area of a degenerate lobe to be much smaller than that of a hyperbolic lobe (but it is not clear that this would be true for all parameter values). It is worth noting that a region of highest stretching discovered by Liu *et al.* (1994) near the walls of a cavity flow may coincide with a mixing region associated with degenerate fixed points at the corners of the cavity (but this hypothesis is difficult to investigate due to limited numerical resolution). Flows with several different mixing regions are highly complex. As yet, insufficient data have been gathered to make general statements on the importance of degenerate mixing regions relative to hyperbolic mixing regions in flows where both are present.

We conclude this subsection by considering a remarkable phenomenon that we have termed *Melnikov resonance*. This phenomenon involves the rapid oscillation of a Melnikov amplitude as a frequency parameter is varied. Melnikov resonance is strikingly apparent in the graph of $F_H(-0.5, \lambda)$ (figure 7b); the graph of $F_H(0.5, \lambda)$ (figure 7a) also exhibits it to a small extent. Owing to the relationships between Melnikov amplitude, lobe area, and size of a mixing region (see (5.4) and §5.5), we expect a positive correlation between $F_H(c, \lambda)$ and the size of the hyperbolic mixing region if it does not intersect the degenerate mixing region. Figure 8 tests this correlation. The first three local extrema of $F_H(-0.5, \lambda)$ occur at $\lambda = 0.060$, 0.110, 0.146. The first of these values of λ caused formidable numerical difficulties; the last
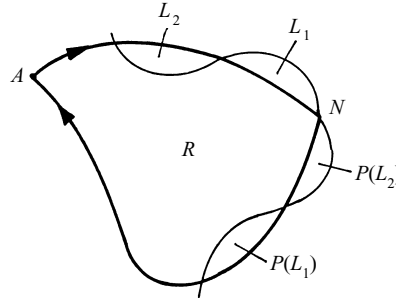
FIGURE 9. Turnstile lobes and their images for the region R associated with the hyperbolic fixed point A. R is bounded by the segments of A_s and A_u from A to N, represented by thicker lines.

two values are used in figure 8. For visual consistency, figure 8 was obtained using $c = 0.5$, $\epsilon = 0.0003$, and oscillating the plate at $x = -1$ (i.e. replacing x in the perturbation term of (2.3) by $-x$); by symmetry, this is equivalent to using $c = -0.5$, $\epsilon = -0.0003$, and oscillating the plate at $x = 1$ as usual. Figure 8 seems to confirm that Melnikov resonance does have implications for the size of a mixing region. At this point, we have no simple explanation for the Melnikov resonance observed in this study. To the best of our knowledge, no other researchers have seen this phenomenon.

5.5. *Lobe dynamics*

The size of a mixing region can be estimated visually by tracing out long segments of invariant manifolds or by long-term Poincaré sections. In this subsection, we show how lobe dynamics (see Wiggins 1992) may be used to compute such an estimate.

First, we consider the case when the hyperbolic and degenerate mixing regions are separate and the degenerate region is bounded. (A separate hyperbolic region is always bounded. We cannot prove that the degenerate region is ever bounded, but Poincaré sections provide some evidence that it often is.) Consider the region R and the lobes L_1 and L_2 in figure 9. L_1 and L_2 may be regarded as 'turnstiles' through which fluid must pass to enter and exit R under the action of P. For small $|\epsilon|$, there are only two pips per period, and so R has only one entry turnstile and one exit turnstile. For larger $|\epsilon|$, there may be two or more entry turnstiles and the same number of exit turnstiles, but the analysis is similar. Note that R was formed using segments of one pair of corresponding half-manifolds of A_s and A_u; an analogous region R', with turnstiles L_1' and L_2', can also be formed using segments of the other pair.

Now, let P^k denote P iterated k times, and define

$$\left.\begin{aligned} L_{0,k} &= \{p \in L_1 \mid P^k(p) \in L_2 \quad \text{but} \quad P^j(p) \notin L_2 \quad \text{for} \quad 0 \leqslant j < k\}, \\ L_{n,k} &= P^n(L_{0,k}) \quad \text{for} \quad 1 \leqslant n \leqslant k. \end{aligned}\right\} \tag{5.5}$$

Clearly, $L_{i,j}$ and $L_{n,k}$ are disjoint unless $i = n$ and $j = k$. Since R is bounded and P preserves area, any fluid which enters R through L_1 must eventually exit R through L_2; such fluid is distinct from fluid which remains forever in R. Thus, letting H denote the hyperbolic mixing region,

$$H \cap R = \bigcup_{k=1}^{\infty} \bigcup_{n=1}^{k} L_{n,k} \quad \text{and} \quad L_1 = \bigcup_{k=1}^{\infty} L_{0,k}.$$

Since $\mu(L_{i,k}) = \mu(L_{j,k})$ *for* $0 \leqslant i, j \leqslant k$, the area of $H \cap R$ is therefore

$$\mu(H \cap R) = \sum_{k=1}^{\infty} k\mu(L_{0,k}) = \mu(L_1) \sum_{k=1}^{\infty} \frac{k\mu(L_{0,k})}{\mu(L_1)}. \tag{5.6}$$

Hence, $\mu(H \cap R)$ is $\mu(L_1)$ times the average transit time from L_1 to L_2. Now, consider the orbits of the lobes L_1 and L_1' under P. It is clear that these orbits intersect and that, in fact, H is the union of these orbits. However, granted the reasonable assumption that P mixes in Aref's *DS* sense in H (see Aref 1991), H is identical (up to a set of measure zero) to the orbit of L_1 (or L_1'). In this case, reasoning like that used to obtain (5.6) shows that $\mu(H \cap R^c)$ is $\mu(L_2)$ times the average transit time from L_2 to L_1, where R^c is the complement of R. Adding this result to $\mu(H \cap R)$ implies, since $\mu(L_2) = \mu(L_1)$, that $\mu(H)$ is simply $\mu(L_1)$ times the average return time for L_1. This average return time can be computed by approximating L_1 by a grid of points and tracking those points under the action of P until they return to L_1, although sensitivity to initial conditions may seriously affect the accuracy of this calculation. In the event that H does not coincide with the orbit of L_1, $\mu(H)$ can still be computed; the revised algorithm would have to estimate the area of the intersection of the orbits of L_1 and L_1'.

To analyse a separate bounded degenerate mixing region D, one can form a region similar to R with turnstiles L_3 and L_4 using segments of B_u, C_s, and the wall at $x = 1$. In this case, it is easy to show that the orbit of L_3 under P covers D and that $\mu(D)$ is $\mu(L_3)$ times the average return time for L_3.

Finally, we consider the case when the hyperbolic and degenerate mixing regions intersect to form a bounded hybrid mixing region Y. If Aref's *DS* mixing occurs in Y, the orbit of L_1 under P coincides with Y, and $\mu(Y)$ is $\mu(L_1)$ times the average return time for L_1. On the other hand, if the orbit of L_1 fails to cover Y, $\mu(Y)$ can still be computed using an algorithm involving L_1, L_1', and L_3.

6. Experimental results and correspondence with theory

In this section, we present the results of our dye advection experiments (see table 2) and compare them with the predictions made in §5. Injection of dye near A should lead to the visualization of the manifold A_u, and injection near B should do the same for B_u. As d is the amplitude of oscillation for the wall, we expect more mixing for $d = 0.5$ cm than for $d = 0.165$ cm.

Recall that the steady streamlines in our experiment 'best match' those of the theoretical flow with $c = 0.54$, even though in our experiment, the effective c is 0.49. To estimate the effects of this non-perfect match, we compared numerically calculated manifolds for $c = 0.54$ and $c = 0.52$, as these c values exhibit steady streamlines that are no more badly matched than are those for $c = 0.54$ and our experimental flow. Cases corresponding to $d = 0.165$ cm exhibited a relatively good match between manifolds, but the match for $d = 0.5$ cm was noticeably poorer. Thus for $d = 0.5$ cm, we do not expect a good match between our experimental results and theory.

Another significant concern is the experimental dye blob, which was larger than the circle of points used to simulate that blob in the Poincaré sections. This probably had little effect near A, where dye leaves the vicinity relatively quickly, but did have a significant effect near B, where the flow is much slower. The larger dye blob caused the dye front to leave the vicinity of B much sooner than was predicted by the Poincaré sections. We correct for this effect when we match dye patterns with Poincaré sections.

Throughout this section, we refer to folded or stretched structures formed by the dye pattern as lobes. These structures are not lobes in the sense of §5, but they do approximate partial boundaries for such lobes.
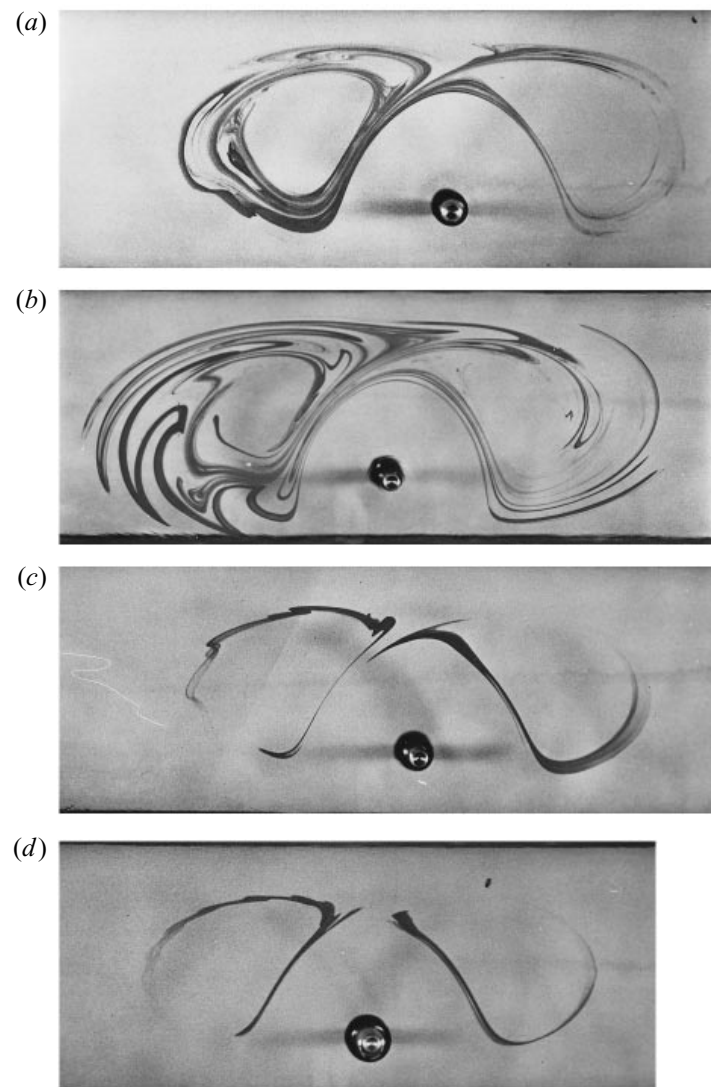
(a)

(b)

(c)

(d)

FIGURE 10. Experimental advection patterns for the dye injected at point A: (a) trial 1 after 19 periods, (b) trial 3 after 17 periods, (c) trial 5 after 7 periods, (d) trial 7 after 13 periods.

Trial	ϵ	λ	d	Injection point
1	0.02	0.406	0.5	A
2	0.02	0.406	0.5	B
3	0.04	0.813	0.5	A
4	0.04	0.813	0.5	B
5	0.02	1.232	0.165	A
6	0.02	1.232	0.165	B
7	0.04	2.463	0.165	A
8	0.04	2.463	0.165	B

TABLE 2. Parameters values for the dye advection experiments

6.1. *Dye advection patterns: early periods*

In §5, the numerically calculated manifolds did not predict characteristics seen in the Poincaré sections after as few as 50 periods. Thus we attempt to match dye traces with these manifolds only for early periods. We begin with trials where $d = 0.165$ cm.

Trials 5 and 7

In both of these trials, dye injected near A was advected and stretched in the directions of A_u, forming two dye fronts. One front began to (approximately) traverse the left-hand loop of the figure-eight steady streamline, and the other began to traverse the right-hand loop. A dye front returning to the vicinity of A after traversing a loop accumulated at A as it split into two fronts, each of which then traversed a separate loop. This behaviour is predicted by theory and was observed whenever we injected dye at A.

In figure 10(c), the dye fronts have each traversed a loop once, and have returned to the vicinity of A. Note that the lobes on the left-hand loop have lengths similar to the lobes seen in figure 6(iii), although the physical lobes are not as large or as sharply defined. Note the absence of pronounced lobe structures on the right-hand loop in both figures. The early behaviour of dye in trial 7 (figure 10d) was similar to that in trial 5. Note that the lobes on the left-hand loop are shorter, smaller, and more numerous than those in figure 10(c), as predicted by figures 6(iii) and 6(iv). For each of these trials, the experimental results correspond well to the computed manifolds.

Trials 6 and 8

In both trials, dye injected near B moved around the rotor, nearly following the steady separating streamline, while some dye remained attached to the wall at B. As the dye front reached the vicinity of C, it accumulated and split into two fronts, one of which began to form a lobe to the left of C as the other continued to circle the rotor. By period 3 of trial 6 (figure 11c), two distinct lobes had formed to the left of C. Note the distinct resemblance to figure 6(iii); the main differences in these figures are the thin lobes encircling the rotor in figure 6(iii) and the fine structure of the lobes to the left of C in figure 11(c). In trial 6 (and all trials in which dye was injected near B), the dynamics near C clearly dominate the stretching and folding process, at least for early periods. The only difference of note in the early behaviour of trial 8 is that the lobes to the left of C are much shorter than those of trial 6, as predicted by figures 6(iii) and 6(iv).

Trials 1 and 3

In both trials, after dye injected at A had made one traversal of the loops, little of the predicted lobe structure was revealed; later in trial 3, this situation changed. For trial 1, figure 10(a) shows the best match to the lobe structure of figure 6(i). Some dye has already traversed the loops at least four times. The top of the left-hand loop in the photograph bears some resemblance to figure 6(i), and most of the lobe formation is taking place on the left-hand loop. Beyond this, there is little resemblance.

In figure 10(b) from trial 3, dye has also made multiple traversals of the loops. Note the remarkable correspondence with figure 6(ii). The left-hand loop has virtually the same outline in both figures, with the exception of the section near the lower right side of the left-hand loop. Clearly the same sorts of dynamics which resulted in the formation of A_u in figure 6(ii) are present. Figure 10(b) and photographs of later periods make it clear that the dynamics around point C are important factors for the
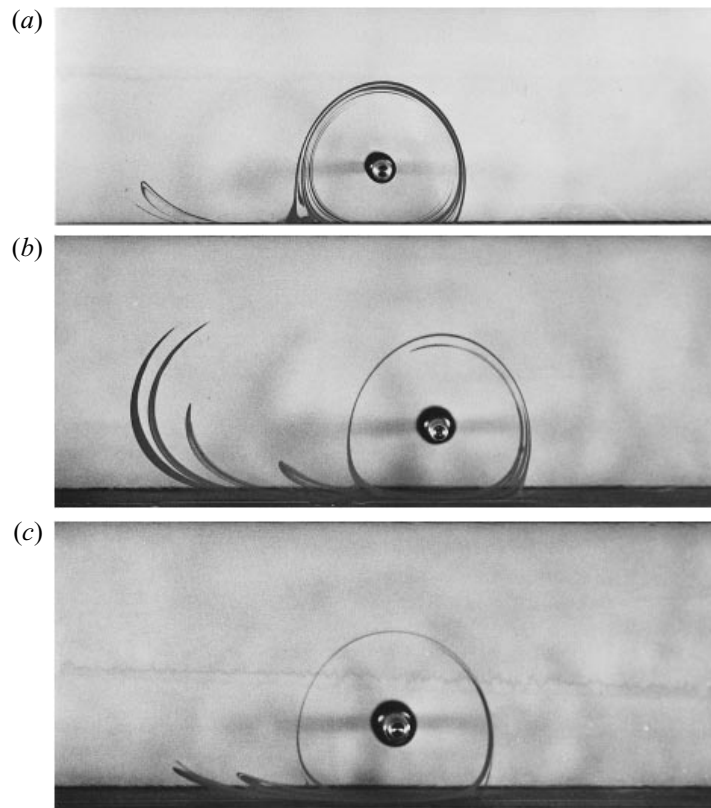
(a)

(b)

(c)

FIGURE 11. Experimental advection patterns for the dye injected at point *B*: (*a*) trial 2 after 2 periods, (*b*) trial 4 after 5 periods, (*c*) trial 6 after 3 periods.

formation of the large lobes bounding the left-hand loop of figure 10(*b*). Thus trial 3 exhibits hybrid mixing, as the stretching and folding of dye depends on the dynamics around both *A* and *C*.

Trials 2 and 4

For trial 2, the best match we obtained with the manifold of figure 6(i) occurred at period 2 (figure 11*a*). Although the lobe to the left of *C* is much larger than that of figure 11(*c*), it is still not as wide as in figure 6(i). There is also more dye encircling the rotor than figure 6(i) predicts. It is likely that a longer unstable manifold plot would account for some of this dye. The trial 4 dye pattern of figure 11(*b*) bears little resemblance to figure 6(ii). We note, however, that the lobes to the left of *C* are shorter than those in figure 11(*a*), which is predicted by figures 6(i) and 6(ii).

6.2. *Dye advection patterns: late periods*

In this subsection, we will be concerned with the match between our experimental results and the Poincaré sections of §5. We will match the shapes and sizes of our dye traces with the 50-period Poincaré sections (figure 4*b*), and we will compare the experimental evidence concerning hybrid mixing with the predictions made by the 500-period Poincaré sections (figure 4*a*).
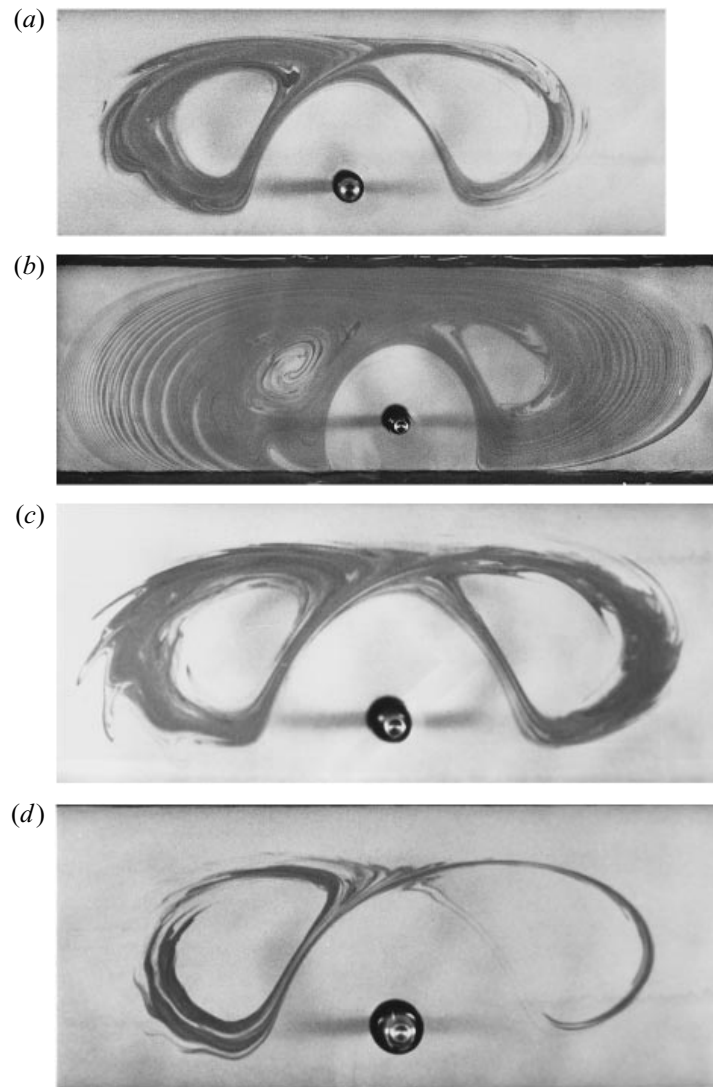
(a)

(b)

(c)

(d)

FIGURE 12. Experimental advection patterns for the dye injected at point A: (a) trial 1 after 52 periods, (b) trial 3 after 50 periods, (c) trial 5 after 53 periods, (d) trial 7 after 51 periods.

Trials 5 and 7

The trial 5 dye trace (figure 12c) is a good match with the corresponding region in figure 4(b)(iii). Note the existence of a large KAM torus in each of the two loops which separates the mixing region from the regular region inside the torus. Also note the lobe-like structures on the left-hand loops of both figures 12(c) and 4(b)(iii).

The left-hand loop of the trial 7 dye trace (figure 12d) is thicker than figure 4(b)(iv) predicts, but is still substantially smaller than the left-hand loop of figure 12(c) (cf. figure 4(b)(iii)). Note the slight undulation visible on the left-hand boundary of the left-hand loop in figure 12(d) (cf. figure 4(b)(iv)). As in trial 5, there are two larger regular regions bounded by KAM tori. The match between experiment and theory is quite good for both of these trials.
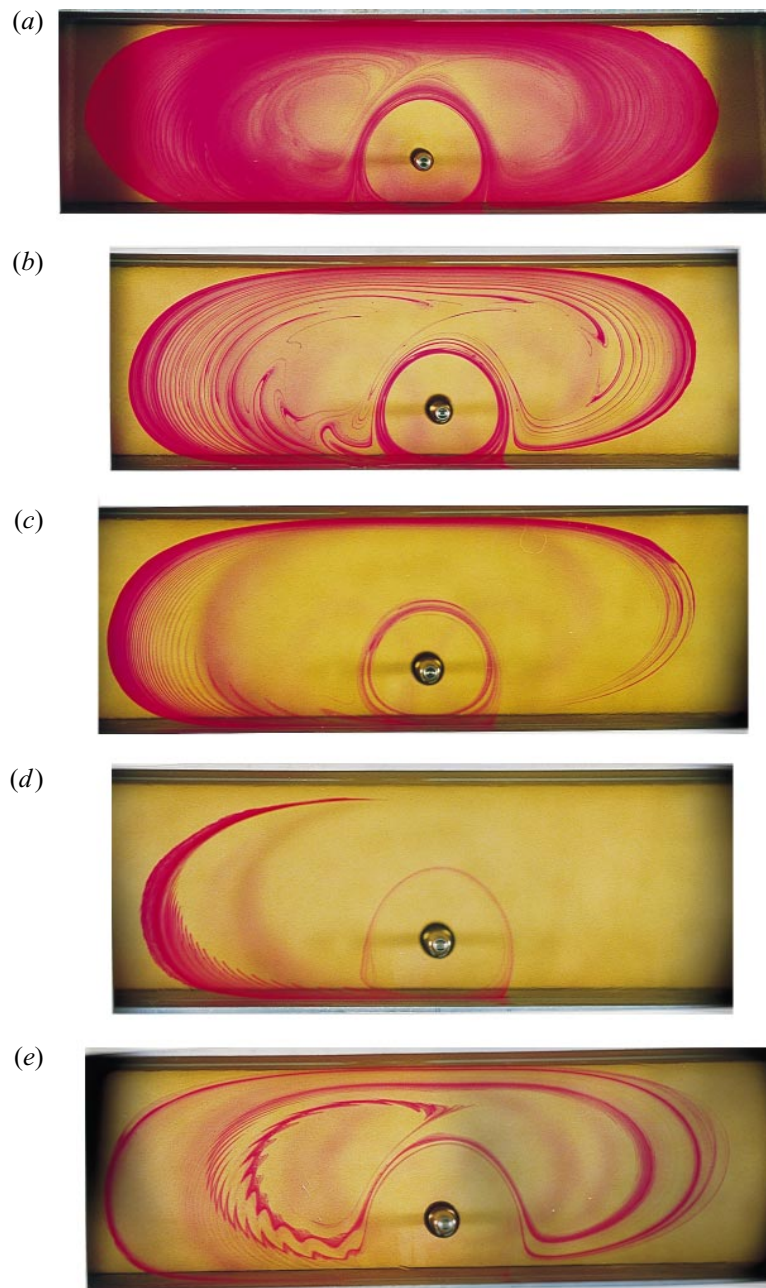
FIGURE 13. Experimental advection patterns for the dye injected at point B: (a) trial 2 after 50 periods, (b) trial 4 after 21 periods, (c) trial 6 after 30 periods, (d) trial 8 after 29 periods, (e) trial 8 after 103 periods.

Trials 6 and 8

As discussed above, the size of the blob injected near B had a profound effect on the rate at which the dye patterns evolved. We will thus match the experimental results (figures 13c and 13d) with the Poincaré sections on the basis of the progression of the dye fronts, and not by the period counts. Both figures 13(c) and 13(d) match the

corresponding parts of figures $4(b)$(iii) and $4(b)$(iv) very well in shape and size. Note that the lobes formed to the left of C move left and out into the tank, where they are stretched lengthwise and the distance between them decreases. When the lobes have circled to a point directly above A, they have been pressed together into a relatively tight stream, which looks solid in the photographs but actually comprises many striations. When the dye front returns to the vicinity of B, the process is repeated.

Figure $12(c)$ and $13(c)$ (trials 5 and 6) suggest that the hyperbolic mixing region and the degenerate mixing region may well overlap, resulting in the formation of a hybrid mixing region, but there is no evidence of overlap at all in figures $12(d)$ and $13(d)$ (trials 7 ad 8) (cf. figures $4(b)$(iii) and $4(b)$(iv)). In trials 5 and 6, the two regions did eventually overlap as predicted by figure $4(a)$(iii). Figure $4(a)$(iv) predicts that the hyperbolic mixing region of trial 7 and the degenerate mixing region of trial 8 will remain separate. This prediction differs from our experiments. In figure $13(e)$, dye has reached the vicinity of point A indicating that hybrid mixing does occur. Note, however, that a computation (see §5.3) involving 2500 iterations of P (only 500 iterations were used in figure $4(a)$(iv)) does predict hybrid mixing in this case.

Trials 1 and 2

For trial 1, the long-term behaviour of dye injected at A turned out to be as problematic as the short-term behaviour. Figure $4(b)$(i) predicts widespread dye advection into regions far from the figure-eight streamline. This was not observed experimentally (figure $12a$). The area of the trial 1 dye trace changed little between periods 36 and 52. Thus we believe a longer experiment would not have lead to significantly more dye spreading.

The results of trial 1 suggest that trial 2 should exhibit only a degenerate mixing region. This was not the case (figure $13a$). Dye has reached the vicinity of point A, and some of the dynamics associated with A can be observed. Thus there is hybrid mixing for the parameters of trials 1 and 2. It is also clear that degenerate mixing (due primarily to the dynamics near C) is considerably more efficient that hyperbolic mixing (due primarily to the dynamics near A) for this set of parameter values.

Trials 3 and 4

In both of these trials, the widespread mixing predicted was observed (figures $12b$ and $13b$). There is very good correspondence between figure $12(b)$ and figure $4(b)$(ii) with one exception. Figure $4(b)$(ii) and figure $4(a)$(ii) both show a small but distinct regular region in the interior of the left-hand loop, presumably bounded by a KAM torus. It is clear from figure $12(b)$ that this torus has broken down, leading to the destruction of the regular region. By symmetry and time reversal, there also cannot be a regular region in the interior of the right-hand loop. Notice that in figure $13(b)$ (trial 4), the dye has already reached the vicinity of A and that dynamics typical of those associated with A can be observed in the dye pattern.

We wish to make one final point regarding our experimental results. In a single experiment, if we had injected dye blobs at any two distinct locations, theory would have prohibited the two dye traces from intersecting, but it would have been possible for dye from the second blob to occupy a location formerly occupied by dye from the first blob, as long as none of that dye still remained. However, dye injected at both A and B should visualize segments of the manifolds A_u and B_u, which cannot cross and are *invariant*. Thus the dye trace from A at period P should not intersect the dye trace from B at period P', for any two periods P and P'. Examine figures $11(b)$ and $12(b)$ in this context. Notice the beautiful fit between the two dye traces, which illustrates the

delicacy of the intertwining of A_u and B_u and gives credence to our claim that it is these manifolds that we are actually visualizing.

7. Conclusions, applications, and future work

The theoretical tools used to study the rotor–oscillator flow were effective for different purposes. Invariant manifolds were useful in determining mechanisms of stretching and folding and in predicting short-term dye patterns, but were of little use in forecasting the extent of mixing regions. Short-term Poincaré sections were good predictors of observed dye patterns, and long-term Poincaré sections were of use in predicting the size and shape of mixing regions, but neither of these gave much information on mixing dynamics. A combination of manifolds and long-term Poincaré sections (as in figure 5c) was valuable for detecting borderline hybrid mixing regions. Melnikov analysis was effective for theoretically establishing the existence of manifold tangling and for estimating the amount of associated mixing. This analysis suggested that in the majority of cases, degenerate mixing was at least as important as hyperbolic mixing. This last observation was confirmed experimentally. In this regard, the ROF appears to differ from the other geometries in which both degenerate and hyperbolic mixing have been studied.

Our results demonstrated that the dynamics near reattachment point C are far more significant for the degenerate mixing than the dynamics near separation point B. This supports a general claim about mixing near such points made by Jana *et al.* (1994a).

Based on our comparison of theoretical and experimental steady flows, it appears that the main source of disagreement between these flows was the non-zero radius of our experimental rotor. We conclude that a line rotlet is generally not a good approximation of a rotating cylinder of small radius when detailed theoretical predictions are required.

After adjusting somewhat for the discrepancies between theoretical and experimental steady flows, the correspondence between theoretical predictions and experimental results in the short-term was generally good for $d = 0.165$ and poor for $d = 0.5$ except in trial 3 which corresponded closely. With respect to long-term behaviour, there were only two significant disagreements between theory and experiment: the results of trials 1 and 8 did not agree with predictions (based on 500-period Poincaré sections) regarding the existence of a hybrid mixing region.

We are pleased with the performance of the sugar solution and tracer in our experimental work. As these materials are much less expensive than more traditional glycerine and dye combinations, we anticipate that others may use these materials in future.

An objective of this paper was to validate various theoretical techniques that we wished to apply to invariant manifolds associated with points B and C. We were able to establish that such manifolds exist, but were unable to prove that Melnikov's method could be applied to them. However, we do provide solid numerical evidence that our use of Melnikov's method for analysing the degenerate heteroclinic tangling associated with B and C is valid.

Regarding the *Melnikov resonance* we observed theoretically, there is some correspondence between the sizes of the lobes predicted by Melnikov analysis and the areas of the mixing regions visualized via Poincaré sections, suggesting that there really is some sort of resonant mixing phenomenon at work here. We have no physical explanation for this phenomenon. It remains an open question whether this resonance

is peculiar to the rotor–oscillator flow or will be seen again by others as different geometries are investigated.

We close with some remarks concerning possible applications and future work. Chaotic dynamics can be exploited in various engineering applications involving mixing and related processes. Ottino *et al.* (1992) discuss, for example, how chaos can be used to improve mixing efficacy, enhance fluid transport, and control aggregation and fragmentation in two-phase flows. Since a rotor (used here in the sense of a rotating impeller of any kind, even three-dimensional) is often used for mixing fluids, the results of this paper are potentially useful for the design of mixing devices.

One insight that can be gained from our work with the rotor–oscillator flow concerns the placement of a rotor inside a mixing vessel; specifically, the rotor–oscillator flow suggests that in some cases the most effective mixing may occur when a rotor is placed fairly close to a wall to create an intense pair of degenerate fixed points (to which stable and unstable manifolds are attached) on the wall. In such cases, the flow could be made chaotic by oscillating the wall, as in the rotor–oscillator flow, or by oscillating the rotor itself in some way. Chaotic advection would also be conveniently induced by using a rotor without circular symmetry; the geometry of the resulting flow would change in a time-periodic way, and so the locations of the degenerate fixed points on the wall (presuming they exist as in the rotor–oscillator flow) would vary periodically with the base phase of the Poincaré map. Most rotors used for practical purposes do not have circular symmetry (e.g. the screw-type rotor used in many washing machines).

The ideas above suggest a fruitful direction for further research: the study of flows driven by rotors without circular symmetry. For example, a flow could employ a rotor with a cross-section consisting of an ellipse or a cross formed by two rectangles intersecting at right angles. Owing to its periodically changing geometry, such a flow would be more difficult to analyse than our rotor–oscillator flow, but efficient and accurate methods do exist for dealing with such flows. One such method, involving the use of boundary integral equations, has recently been used by Jana, Tjahjadi & Ottino (1994*b*) to examine a low-Reynolds-number cavity flow with a moving baffle. It would also be worthwhile to investigate mixing by rotors in two-dimensional flows with moderate Reynolds numbers. The techniques employed by Shariff, Pulliam & Ottino (1991) to analyse the time-periodic wake of a circular cylinder may be useful in this regard. The final (daunting) step in the study of mixing by rotors would be an investigation of rotors (such as screw-type or propellor-type rotors) which generate three-dimensional flows.

Our work with the rotor–oscillator flow suggests the design for a continuous throughput mixing device which we term the *rotor–channel mixer*. This consists of a channel through which fluid is pushed by a pressure gradient and in which fluid is mixed by a series of rotors (without circular symmetry) placed alternately on each side of the channel with their axes perpendicular to the surface of the fluid. It seems likely that the rotor–channel mixer would be effective for mixing chemical or biological reactants suspended in a viscous medium. Optimal placement of the rotors, in order to minimize regular regions or maximize mixing efficiency, could be investigated. The work of Ottino *et al.* (1992) on symmetries in duct flows suggests that mixing in the rotor–channel mixer will be more effective when the arrangement of rotors in the channel is spatially aperiodic (although the analogy between our rotor–channel mixer and a duct flow is somewhat tenuous). One can also imagine a mixing device based on a duct flow in which rotors are placed at various locations along the length of the duct with their axes parallel to the duct axis.

Finally, it should be remarked that although the most effective mixing flows are

turbulent, there are nonetheless many cases where mixing by chaotic advection in a laminar flow may be preferable. Some of these cases involve the mixing of fluids of such high viscosity that the power input required for turbulence is excessive. Other cases occur in bioprocess engineering. Mammalian cells (unlike single-cell microbes) are highly susceptible to damage by shear stresses since they lack a rigid cell wall (Smith 1994); the design of tissue culture reactors is restricted by the degradation to such cells caused by phenomena such as eddy stresses and cavitation associated with turbulence (Charles & Wilson 1994). Moreover, highly agitated and aerated reactors are prone to foaming which can obstruct transport and reactor operation (Shah 1992). In sum, it is evident that chaotic advection can be profitably applied in engineering settings. We must concur, however, with Ottino *et al.* (1992) in their assertion that the onus is now on engineers to incorporate the ideas of chaos into new technology.

REFERENCES

AREF, H. 1984 Stirring by chaotic advection. *J. Fluid Mech.* **143**, 1–21.

AREF, H. 1991 Stochastic particle motion in laminar flows. *Phys. Fluids* A **3**, 1009–1016.

AREF, H. & BALACHANDAR, S. 1986 Chaotic advection in a Stokes flow. *Phys. Fluids* **29**, 3515–3521.

BALLAL, B. Y. & RIVLIN, R. S. 1976 Flow of a Newtonian fluid between eccentric rotating cylinders: inertial effects. *Arch. Rat. Mech. Anal.* **62**, 237–294.

CHAIKEN, J., CHEVRAY, R., TABOR, M. & TAN, Q. M. 1986 Experimental study of Lagrangian turbulence in a Stokes flow. *Proc. R. Soc. Lond.* A **408**, 165–174.

CHARLES, M. & WILSON, J. 1994 Fermentor Design. In *Bioprocess Engineering: Systems, Equipment and Facilities* (ed. B. K. Lydersen, N. A. D'Elia & K. L. Nelson), pp. 5–64. Wiley.

CHIEN, W.-L., RISING, H. & OTTINO, J. M. 1986 Laminar mixing and chaotic mixing in several cavity flows. *J. Fluid Mech.* **170**, 355–377.

GUCKENHEIMER, J. & HOLMES, P. 1983 *Nonlinear Oscillations, Dynamical Systems, and Bifurcations of Vector Fields.* Springer.

HACKBORN, W. W. 1990 Asymmetric Stokes flow between parallel planes due to a rotlet. *J. Fluid Mech.* **218**, 531–546.

JANA, S. C., METCALFE, G. & OTTINO, J. M. 1994*a* Experimental and computational studies of mixing in complex Stokes flows: the vortex mixing flow and multicellular cavity flows. *J. Fluid Mech.* **269**, 199–246.

JANA, S. C., TJAHJADI, M. & OTTINO, J. M. 1994*b* Chaotic mixing of viscous fluids by periodic changes in geometry: baffled cavity flow. *AIChE J.* **40**, 1769–1781.

KAPER, T. J. & WIGGINS, S. 1993 An analytical study of transport in Stokes flows exhibiting large-scale chaos in the eccentric journal bearing. *J. Fluid Mech.* **253**, 211–243.

LEONG, C. W. & OTTINO, J. M. 1989 Experiments on mixing due to chaotic advection in a cavity. *J. Fluid Mech.* **209**, 463–499.

LIU, M., PESKIN, R. L., MUZZIO, F. J. & LEONG, C. W. 1994 Structure of the stretching field in chaotic cavity flows. *AIChE J.* **40**, 1273–1286.

MOFFATT, H. K. 1964 Viscous and resistive eddies near a sharp corner. *J. Fluid Mech.* **18**, 1–18.

OTTINO, J. M., MUZZIO, F. J., TJAHJADI, M., FRANJIONE, J. G., JANA, S. C. & KUSCH, H. A. 1992 Chaos, symmetry, and self-similarity: exploiting order and disorder in mixing processes. *Science* **257**, 754–760.

PARKER, T. S. & CHUA, L. O. 1989 *Practical Numerical Algorithms for Chaotic Systems.* Springer.

ROM-KEDAR, V., LEONARD, A. & WIGGINS, S. 1990 An analytical study of the transport, mixing and chaos in an unsteady vortical flow. *J. Fluid Mech.* **214**, 347–394.

SHAH, Y. T. 1992 Design Parameters for mechanically agitated reactors. In *Advances in Chemical Engineering*, vol. 17 (ed. J. Wei, J. L. Anderson, K. B. Bischoff & J. H. Seinfeld), pp. 1–196. Academic.

SHARIFF, K., PULLIAM, T. H. & OTTINO, J. M. 1991 A dynamical systems analysis of kinematics in the time-periodic wake of a circular cylinder. *Lect. Appl. Maths* **28**, 613–643.

SMITH, G. L. 1994 Large-scale animal cell culture. In *Bioprocess Engineering: Systems, Equipment and Facilities* (ed. B. K. Lydersen, N. A. D'Elia & K. L. Nelson), pp. 70–82. Wiley.

SWANSON, P. D. & OTTINO, J. M. 1990 A comparative computational and experimental study of chaotic mixing in viscous fluids. *J. Fluid Mech.* **213**, 227–249.

WIGGINS, S. 1988 *Global Bifurcations and Chaos: Analytical Methods*. Springer.

WIGGINS, S. 1992 *Chaotic Transport in Dynamical Systems*. Springer.

YUSTER, T. & HACKBORN, W. W. 1997 On invariant manifolds attached to oscillating boundaries in a flow. *Chaos* (Submitted).